Unstructured Overset Grid Adaptation for Rotorcraft Aerodynamic Interactions

Rajiv Shenoy * Marilyn J. Smith †
School of Aerospace Engineering, Georgia Institute of Technology
Atlanta, Georgia 30332-0150

A new adaptation strategy is presented that permits time-dependent anisotropic adaptation for dynamic overset simulations. The current development permits adaptation to be executed over a periodic time window in a dynamic flow field so that an accurate evolution of the unsteady wake may be obtained within a single unstructured methodology. Unlike prior adaptive schemes, this approach permits grid adaptation to occur seamlessly across any number of grids that are overset, excluding only the boundary layer to avoid surface manipulations. Demonstrations on rotor-fuselage interactions, including flow field physics, time-averaged and instantaneous fuselage pressures, and wake trajectories are included. The ability of the methodology to improve these predictions without user intervention is confirmed, including simulations that confirm physics that have before now, not been captured by computational simulations. The adapted solutions exhibit dependency based on the choice of the flow field feature-based metric and the number of adaptation cycles, indicating that there is no single best practice for feature-based adaptation across the spectrum of rotorcraft applications.

Introduction

The resolution of unsteady wake features is essential for a multitude of aeroelastic applications pertinent to rotorcraft. These include, but are not limited to modeling of aeroelastic rotor blades in forward flight, rotor-fuselage or rotor-rotor interaction, helicopter-ship interaction, and tail buffet. Other applications of interest can include wing-store separation, ship-wake interactions, and wind turbines. The current most popular computational fluid dynamics (CFD) approach to resolve these multiple reference frame applications is via overset grids, where the moving body or component meshes are generally highly refined and overset on one or more static background grids (Refs. 1–5). Despite the ability of unstructured overset methods to model dynamic bodies, it does not address the issue of numerical dissipation that can result in inaccuracy of the wake physics (Refs. 5,6).

Feature-based grid adaptation for unsteady problems has been applied on single grids using various methodologies. Accurate predictions of hovering rotors in a single rotating adaptive mesh have been performed by several researchers (Refs. 7–10). However, these scenarios can not be immediately applied to the prediction of rotors in forward flight, where adaptation is needed in both the background inertial reference frame and the near-body rotating frame. Further, the interaction of rotors with non-moving bodies such as fuselages, wind-tunnel struts, and other configurational components also require moving-grid capability to simulate multiple motion frames. As an alternative to the overset configuration, Park and Kwon (Ref. 11) have demonstrated an unstructured sliding mesh approach where a rotating grid communicates with a stationary background grid. Here, articulation of the rotor blades was made possible using grid deformation based on a spring analogy, and also applies feature-based grid adaptation. Another non-overset based approach has been described by Cavallo et al. (Ref. 12), which uses unstructured grid movement and deformation to enable moving body adaptation.

Past research efforts in overset adaptation have in many instances relied on an off-body (background) Cartesian grid-based adaptive capability. Meakin (Ref. 13) presented a grid component grouping algorithm with overset structured grids using a method of adaptive spatial partitioning and refinement and applied it to background Cartesian grids. Variations of this technique have been subsequently demonstrated by Henshaw and Schwendeman (Ref. 14) and Kannan and Wang (Ref. 15). Canonne et al. (Ref. 16) used an overset structured cylindrical grid topology to simulate rotor motion in hover where the background grid is adapted. Hybrid-solver developmental efforts have focused on rotor methodologies where two separate solvers are applied in the near body and background regions, respectively. Duque et al. (Ref. 17) have employed a structured near-body and unstructured wake grid approach to evaluate rotors. Here, isotropic adaptation was applied on the un-

*Graduate Research Assistant, Corresponding Author, rajiv.shenoy@gatech.edu, (404)894-3018
†Associate Professor
Presented at the American Helicopter Society 67th Annual Forum, Virginia Beach, VA, May 3-5, 2011.

structured background grid operating in a non-inertial reference frame. This work recommended the use of anisotropic adaptation to accurately capture inherently anisotropic phenomena such as tip-vortices and to exploit computationally efficiency of this grid adaptation technique. Park and Darmofal (Ref. 18) introduced a parallel anisotropic adaptation capability for non-overset tetrahedral grids. This technique has been applied to investigate several applications such as sonic-boom propagation (Refs. 19, 20), viscous transonic drag prediction (Ref. 19), and re-entry vehicle configurations (Ref. 21). Recent development has focused on the coupling of a body-fitted unstructured solver with a high-order Cartesian solver to propagate the wake in the mid and far fields. Sankaran et al. (Ref. 22) and Wissink et al. (Refs. 23, 24) have successfully implemented automatic mesh refinement (AMR) in the Cartesian background solver to resolve the wake based on flow field features.

The effect of time-dependency on the flow field is an essential aspect in applying grid adaptation to study dynamic moving bodies. Researchers (Refs. 12, 16) have shown that adapting the solution at a given frequency (based on flow time) have proven effective, with increasing frequency yielding higher accuracy. Investigations involving off-body Cartesian-based adaptive mesh refinement (Refs. 14,15,22–24) have extended this rationale to adapt the solution a frequency comparable to that of the solver time step, allowing for a coupled adaptive flow solver. However, this capability is not computationally efficient for tetrahedral unstructured-based methods as they do not have the advantage of octree data structures to provide for the adaptive mechanics.

An alternative approach is thus required which addresses the time-dependency issue without the computational overhead of frequent adaptation. Kang and Kwon (Ref. 8) present an adaptation technique that detects local maxima of a vortex core every five degrees and using a 3-D parabolic blended curve to represent the vortex core path. Park and Kwon (Ref. 11) describe a 'quasi-unsteady' adaptive procedure for rotors in forward flight based on a time period or window dependent on the blade passing frequency. Cells satisfying an adaptation indicator are marked at each time step within the window and adaptation is performed for those cells at the conclusion of each window. Sterenborg et al. (Ref. 25) describes a similar technique and applied it for a fluid-structure interaction investigation. The extension of a time-dependent feature-based adaptation methodology for anisotropic grids involving dynamic bodies is delineated by Alauzet and Oliver (Ref. 26).

These successful implementations of grid adaptation provide impetus for further investigation of this approach for rotorcraft applications involving multiple grids. What is common across these prior overset-based efforts is that the adaptation is restricted to the off-body background meshes. Since vorticity originates on a viscous surface where the near-body grid is employed, the full capability of the adaptation cannot be exploited unless the adaptation can occur across the meshes. In addition, for rotorcraft configurations, a time-dependent strategy is necessary to permit accurate and efficient simulation of the wake growth.

This paper presents a new adaptation strategy that permits time-dependent anisotropic adaptation for dynamic overset simulations. Since an unstructured background grid can encompass many complex stationary bodies (e.g. fuselage, nacelle, and tower) the overset grid refinement complexity inherent in a structured grid-based approach is avoided. The current development dictates adaptation to be executed over a periodic time window in a dynamic flow field so that an accurate evolution of the unsteady wake may be obtained within a single unstructured methodology.

Two configurations that continue to elude accurate simulation in one or more areas with current CFD methods were chosen to evaluate the new adaptation strategy. These two configurations fall under the category of rotor-fuselage interaction (RFI), an aeroelastic phenomenon that is characterized by an unsteady rotor wake impinging on an inertial fuselage. These two cases permit both inviscid and viscous options to be rapidly evaluated.

Methodology

Flow Solver

FUN3D, NASA's unstructured RANS solver, was selected as the flow solver with which to demonstrate the new adaptation strategy. FUN3D utilizes an implicit, node-based finite volume scheme to resolve the RANS equations on unstructured, mixed-topology grids (Ref. 27).Both compressible and incompressible (Ref. 28) Mach regime capabilities are available in the flow solver. Time-accuracy is achieved using a second-order backward differentiation formula (BDF). Roe's flux difference splitting scheme (Ref. 29) is used compute the inviscid fluxes, while an equivalent central difference approximation is utilized to resolve the viscous fluxes. A Gauss-Seidel strategy is used to solve the resulting linear system of equations. FUN3D has available a plethora of turbulence methods available, of which Menter's kω-SST (Ref. 30) 2-equation model was applied in this effort. SUGGAR++ (Ref. 31) and DiRTlib (Ref. 32) provide overset capability with FUN3D and have been successfully used for compressible and incompressible rotorcraft applications (Refs. 3,5). In such simulations, the background grid, which consist of the fuselage and other wind-tunnel static geometries up to the far-field boundaries, are assembled with finer near-body grids for each of the moving rotor blades.

Anisotropic Feature-Based Adaptation

FUN3D's anisotropic tetrahedral adaptation capability (Refs. 18, 33) formed the basis for the new adaptation strategy. This feature-based adaptation requires the identification of a feature, as well as an algorithm or key to define the

grid modification. In this effort, several different features were explored, including vorticity and pressure gradients. The vorticity adaptation key, $K_{e,\omega}$, is similar to the one successfully applied by (Ref. 17), which scales vorticity (ω) with an edge length, ℓ_e. The formulation of the vorticity-based key for a given edge connecting nodes $n1$ and $n2$ is computed for the averaged vorticity magnitude across the edge,

$$K_{e,\omega} = \ell_e \frac{|\omega|_{n1} + |\omega|_{n2}}{2}. \tag{1}$$

A comparable pressure gradient key, $K_{e,p}$, was also defined as the magnitude of the pressure gradient Δp scaled by the length of the cell edge (ℓ_e) as

$$K_{e,p} = \ell_e |\Delta p|. \tag{2}$$

Using one of these keys, the normalized local adaptation intensity, $\hat{I}$, is derived for each node as the maximum of the edge key, K_e, over all incident edges of a given node,

$$\hat{I} = \max_{edges} \left(\frac{K_e}{K_t} \right), \tag{3}$$

where K_t is a user-specified tolerance. The new isotropic mesh spacing is calculated using an estimate of the spacing on the original mesh h^0, a coarsening factor C (typically around 115%), and the adaptation intensity by,

$$h_1 = h^0 \min \left(C \left(\frac{1}{\hat{I}} \right)^{0.2} \right), \tag{4}$$

Consequently, an anisotropic adaptation metric may be derived using a scalar quantity for the isotropic spacing and a Hessian to stretch the resulting mesh. The Hessian of a quantity $(-)$ can be described as

$$H = \begin{bmatrix} \frac{\partial^2(-)}{\partial x^2} & \frac{\partial^2(-)}{\partial x \partial y} & \frac{\partial^2(-)}{\partial x \partial z} \\ \frac{\partial^2(-)}{\partial x \partial y} & \frac{\partial^2(-)}{\partial y^2} & \frac{\partial^2(-)}{\partial y \partial z} \\ \frac{\partial^2(-)}{\partial x \partial z} & \frac{\partial^2(-)}{\partial y \partial z} & \frac{\partial^2(-)}{\partial z^2} \end{bmatrix}. \tag{5}$$

Further details of the computation Hessian-based metric and its significance to the adaptation process are delineated in (Ref. 33). The vorticity-based adaptation invokes the vorticity-magnitude Hessian to determine anisotropy, while the pressure gradient adaptation utilizes the Mach number Hessian, described in (Ref. 21).

Extension to Overset Grids

The overset grid adaptation capability does not restrict adaptation to any component grid. This enables each grid to evolve independently and, in general, ensures for an orphan free composite grid. The current adaptation capability for viscous flows is restricted only to nodes beyond the boundary layer. FUN3D applies an adaptation software module that computes the adaptation metric as well as handles all associated adaptive mechanics. Description of the parallelized adaptation mechanics, which include grid operations such as node insertion and removal by splitting or collapsing edges, edge and face swapping, and node smoothing are detailed in Ref. 33. The extension of this method to include overset adaptation requires communication with DiRTlib (Ref. 32), the grid connectivity module, to assign a component mesh ID for each node in the composite mesh. The code performs adaptation over the entire composite grid system by tracking the component mesh ID for all added nodes.

Since overset assembly of the component meshes is handled by a library outside of the FUN3D framework (SUGGAR++) (Ref. 31), a generalized global index convention was requisite so that subsequent assembly of the adapted grid with its domain connectivity information would be compatible with the solution information. This process is required to perform valid solution transfers between the unadapted and adapted grid systems. The convention requires both the flow solver and adaptation code to assign composite grid global indexes by arranging nodes in contiguous fashion by mesh ID over the list of component meshes. Nodes added due to adaptation are initially assigned new global indexes by appending them to the current global index list. Node removal results in unused global indexes, which is handled by a reverse, global-index shifting procedure. In order to satisfy the condition of contiguous mesh IDs, a new procedure was introduced to re-sort the global indexes of the adapted grid system as illustrated in Fig. 1. After adaptation, the component meshes are then saved, and the resultant domain connectivity information is obtained by invoking SUGGAR++ for subsequent grid assembly.

Mesh ID	Original Node Indexes	Updated Node Indexes	New Node Indexes
1	1 2 ~~3~~	1 2	14 15
2	4 ~~5~~ 6	3 4	16
3	7 8 9	5 6 7	17
4	~~10~~ 11 12	8 9	18 19 20
5	13 14 15 ~~16~~ 17	10 11 12 13	21

(a) Node removal (struck through) and insertion

Mesh ID	Updated Node Shifted Indexes	New Node Shifted Indexes
1	1 2	3 4
2	5 6	7
3	8 9 10	11
4	12 13	14 15 16
5	17 18 19 20	21

(b) Resorted global indexes

Fig. 1. Global index convention illustrated for an example overset grid system.

Time-Dependent Adaptation

Time-dependent adaptation is obtained using a methodology based on that developed by Alauzet and Olivier (Ref. 26). The anistropic grid metric is computed for every grid node at a given time step and is progressively intersected over a selected time window such that the strongest restrictive metric at each node is retained to form the time-dependent grid metric. The Hessian, H, is intersected in time by collecting N solution samples within a time window w as given by,

$$|H_{w,max}| = \bigcap_{n=1}^{N} |H_{w,n}|, \tag{6}$$

Using the resulting metric, a new adapted mesh may be obtained suitable for multiple time intervals characterized by the flow phenomena obtained within the adaptive window. For rigid-body rotorcraft simulations, such a window is identified as the time corresponding $1/n_{blades}$ revolutions. In this study, the solution is sampled at each time step throughout the time window to obtain the metric intersection. The present approach does not utilize a solution transfer capability; hence, the inherent solver accuracy is retained as a result of re-simulation of the unsteady physics.

Georgia Institute of Technology (GIT) RFI Demonstration Case

The GIT fuselage configuration is comprised by a cylindrical fuselage and a hemispherical nose to permit easier identification of RFI has been extensively evaluated in the Harper Wind Tunnel (Ref. 34). The rotor blades have a rectangular planform with a NACA-0015 airfoil section. The rotor blades are nearly rigid which allow for CFD analyses that neglect structural deformations. Two advance ratios ($\mu = 0.10$ and $\mu = 0.20$) are selected for investigation and the relevant blade angles and thrust are reported in Table 1. Data from this effort include instantaneous and time-averaged pressures along the fuselage, as well as vortex behavior via laser light sheets. The fuselage length is non-dimensionalized (x/R) by the rotor radius ($R = 457mm$) for ease in presentation.

This model has been evaluated by numerous prior computational efforts with a variety of approaches, for example Refs. 1, 2, 35–37. O'Brien (Ref. 3) used this as a validation case for his series of actuator to overset rotor models implemented into FUN3D. Numerous details of the time-averaged fuselage pressure coefficient have not been captured by these methods, in spite of the simplistic model geometry. O'Brien (Ref. 3) noted that some time-averaged features just aft of the rotor were captured when the entire model (rotor strut and hub) were included, which prior efforts neglected. However, the vortex interaction observed in the original experiments near the nose (x/R 0.3) (Ref. 34) has not been adequately resolved by any of these prior simulations.

Table 1. Blade angles and resulting thrust obtained for GIT test cases. (Note: All angles are reported in degrees.)

μ	β_{1s}	β_{1s}	C_T
0.10	-2.02	-1.94	0.009045
0.20	-2.62	-3.29	0.009950

Simulations were computed using the compressible, inviscid equation set as separation and other viscous effects should be minimal for the configurations chosen. Solution advancement was performed with a time step equivalent to 1° azimuthal sweep. During each time-step, 25 sub-iterations were used in conjunction with the temporal error control option to ensure 1-2 orders of magnitude reduction in residual. The metric intersection was performed over a time window corresponding to 180° blade sweep or 180 steps after the solution became periodic (after 2 revolutions). In order to obtain valid comparisons with experiment, the thrust values obtained for these cases were ascertained to be within 1% of those listed in Table 1.

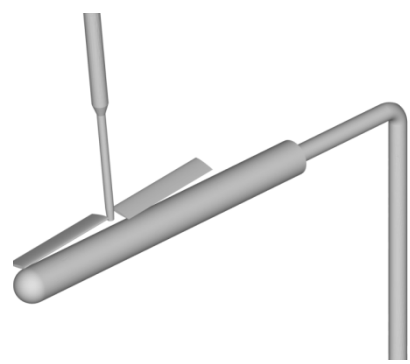

Fig. 2. Model of the GIT rotor-airframe configuration.

Several feature-based adaptations were evaluated for the GIT RFI model to determine the validity of the method, as well as the appropriate flow field metric. The $\mu = 0.1$ case was examined first, and the most successful metrics were determined to be the vorticity magnitude and pressure gradient, as shown in Table 2. The pressure gradient adaptation (Scheme C), resulted in a much more efficient adaptation than the vorticity magnitude (Scheme B), as denoted by the mesh node count. Only minor differences between these two metrics were observed for the time-averaged fuselage pressure coefficient peaks at the $x/R = 0.5$ and 2.0 locations (Fig. 3) after one cycle. The result of the first adaptation was to refine the initial vortex interaction at the nose ($x/R = 0.1$), so that the magnitude and pressure rise are more adequately captured. The effects of the vortex shed from the second blade, observed in the pressures along

Table 2. Summary of the different adaptation metrics for the GIT configuration at $\mu = 0.1$

Scheme	Description	Grid Size
A	Initial Grid	2.03M nodes
B	Adapted to $\|\omega\|$ (1 cyc.)	6.68M nodes
C	Adapted to ∇p (1 cyc.)	2.92M nodes
D	Adapted to $\|\omega\|$ (2 cyc.)	12.8M nodes
E	Adapted to $\|\omega\|$ (1 cyc.) & ∇p (1 cyc.)	8.86M nodes

$x/R = 0.2 - 0.5$, are not captured with either the baseline or the single adaptation. The vortex-fuselage interaction at $x/R = 2.3$ is captured by all three meshes as a weak pressure pulse, and the magnitude does not change with grid adaptation, although a minor ($x/R < 0.05$) shift forward is observed upon mesh adaptation.

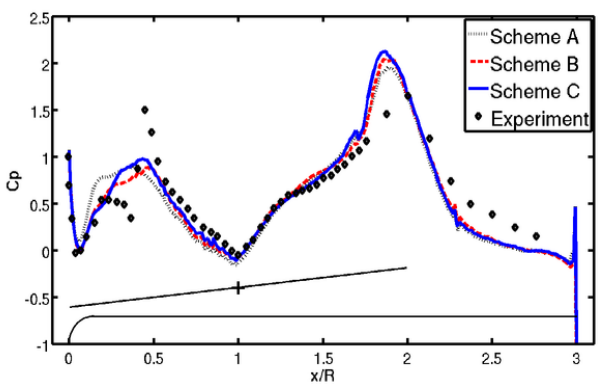

Fig. 3. Comparison of the time-averaged pressure distributions on the top centerline of the GIT airframe resulting from 1 adaptive cycle for $\mu = 0.1$.

A second adaptation cycle was performed on the two metrics singly, as well as a cross adaptation (Table 2). The results of the second adaptation are much more significant (Fig. 4). For clarity, the double adaptation with pressure gradient is not shown as it is similar to that of the double adaptation with the vorticity magnitude (Scheme D). While the double adaptation on the single metric results in a much larger mesh size, its influence on the fuselage pressure characteristics is minimal. Conversely, adaptation on the vorticity magnitude, followed by a second adaptation on the pressure gradient (Scheme E) yields significant improvement, and employs about 75% of the mesh required by Scheme D. While the pressure rise associated with the vortex from the second blade is greater than the experimentally measured value, the fuselage-vortex interaction described by Brand (Ref. 34) and denoted by the sharp rise in pressure between $x/R = 0.4 - 0.5$ is captured.

Further examining the instantaneous flow field (Figs. 5 - 9), the characterizations noted in the time-average pressures are re-enforced in these data. For the first quarter revolution where the rotor blades approach and pass over the fuselage (Ref. 5), the single and double adaptations on vorticity magnitude (Schemes B and D) improve the instantaneous pressure prediction only slightly, and include a significant lag ($x/R = 0.05 - 0.1$) in the location of the fuselage interaction at $x/R = 0.4 - 0.5$. The mixed double adaptation (Scheme E) still encounters some issues with magnitude ($\psi = 30^\circ$ and 60°) and a shift in phase of this vortex interaction, particularly at $\psi = 90^\circ$, however the results are significantly improved over the single adaptation. It is also important to note that the magnitude and character of the pressure rise resulting from the vortex-fuselage interaction, which is completely missed by the baseline and other adaptation schemes, are overall well-captured. Minor differences are observed in the centerline pressure exclusive of this vortex interaction.

The second quarter of the rotor revolution continues overall this trend, but with increasing differences with experiment as the two rotor blades move past the fuselage to their original positions. Again the vortex interaction at $x/R = 0.4 - 0.5$ continues to be better captured with Scheme E. The experimentally observed vortex-fuselage interaction between $x/R = 0.7 - 0.9$ during this quarter is not captured by the vorticity adaptation. The mixed vorticity magnitude-pressure gradient adaptation appears to capture this feature early and as a weaker interaction at $\psi = 120^\circ$ and 150°. The significant over pressure near the nose ($x/R = 0.2$) at $\psi = 180^\circ$ when the blades are directly over the fuselage is not predicted using any method, indicating that additional refinement and viscous effects may be important at this location. Once again, however, it is evident that the mixed adaptation (Scheme E) preserves more of the flow features.

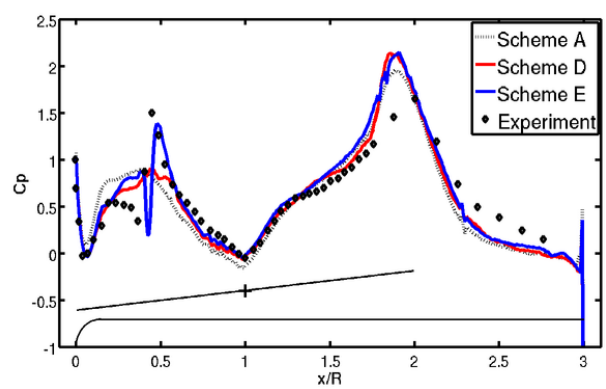

Fig. 4. Comparison of the time-averaged pressure distributions on the top centerline of the GIT airframe resulting from 2 adaptive cycles for $\mu = 0.1$.

To further understand the significance of the grid refinement in each scheme, the vortex behavior is examined in Figs. 7 – 9. The schemes A–E (Fig. 2), are plotted from top to bottom at each selected azimuthal location. It is

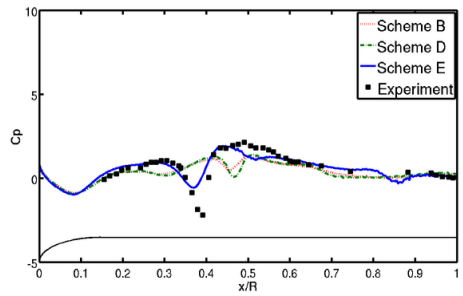

(a) $\psi = 30°$

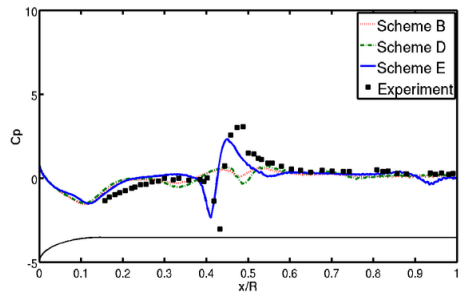

(b) $\psi = 60°$

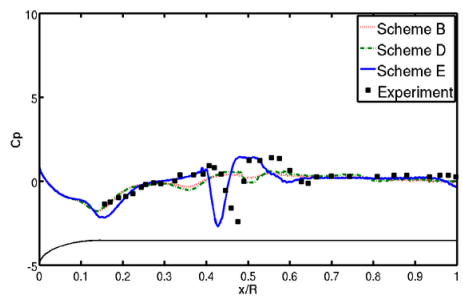

(c) $\psi = 90°$

Fig. 5. Comparison of instantaneous pressure distributions on the top centerline of the GIT airframe for $\mu = 0.1$ (first quarter revolution).

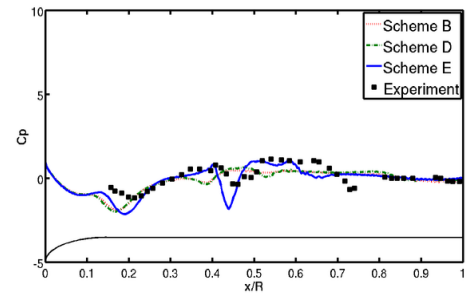

(a) $\psi = 120°$

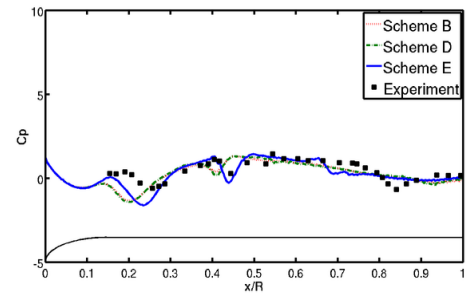

(b) $\psi = 150°$

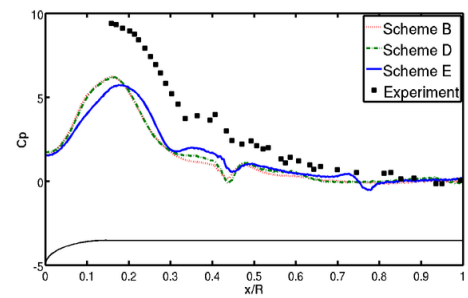

(c) $\psi = 180°$

Fig. 6. Comparison of instantaneous pressure distributions on the top centerline of the GIT airframe for $\mu = 0.1$ (second quarter revolution).

clear from scanning from top to bottom that the vortex core is more crisply predicted after one adaptation (second and third plots) and refined further after the second adaptation (fourth and fifth plots). In addition, weak vorticity interacting with the fuselage, spread over large areas, become further defined with the adaptation. In Fig. 9 (b), at $\psi = 180°$ where the blade is present over the fuselage centerline, the blade-vortex interaction is clearly captured with the mesh adaptation in the near-body and fuselage grids.

Differences between the various adaptation schemes can also be discerned from the magnitude and shape contours of the vorticity in these figures. For example, the shape of the vorticity between $x/R = 0.4 - 0.5$ where the first fuselage-vortex interaction occurs is very different. Specifically, tracing Scheme E (the bottom plot) across Figs. 7 – 9, it is possible to discern the path of the tip vortex as it leaves the blade, interacts with the blade root vortex, and finally collides with and encompasses the fuselage centerline.

Brand (Ref. 34) reported that the tip vortex from the prior blade could be observed at $x/R = 0.3$ at $\psi = 188°$, which is comparable to the grid adaptation results in Fig. 9 (b). As the blade moves across the fuselage, Brand reports that the vortex weakens (remaining approximately stationary about $x/R = 0.3$), while the vortex sheet from the blade passage is swept downstream. By $\psi = 225°$, Brand notes that "... vortex sheet appears to generate a region of circulatory flow with a sense opposite to the tip vortex " and "...for $\psi = 224°$ where the vortex sheet is no longer visible, but the remnant of the streakline appears to swirl as it travels rapidly downstream along the top of the airframe." This correlates to the azimuths between Figs. 7 a) and b), where weak vorticity is observed at approximately $x/R = 0.3$, correlating to the remnants of the preceding blade's tip vortex. The vortex sheet roll-up, which was experimentally observed to travel between $x/R = 0.4 - 0.5$ during this azimuthal time period can also been observed traveling downstream at $\psi = 30°$

(or $\psi = 210°$) and with a distinct rotation by $\psi = 60°$ (or $\psi = 240°$), located in the same fuselage locations.

Brand's observations describe the development of the secondary, downstream fuselage-vortex interaction that are also observed in Scheme E, unlike the other adaptation schemes. Unfortunately, further experimental evaluation of this vortex and its interaction with the fuselage were not provided in Ref. 34. The track of the vortex is clearly observed throughout the azimuthal sequence after its development. The lack of correlation for the fuselage centerline pressure between the experiment and Scheme E (Fig. 5) appears to be due to the height of the vortex above the fuselage, which can be attributed to the nature of the inviscid CFD calculations.

The ability of the new scheme to capture complex unsteady features in the flow field is confirmed in Fig. 10. The top figure (Scheme A) illustrates the baseline grid, and the distinction between the background and blade grids can be easily observed. After one adaptation (Scheme B), the blade vortex interaction is more more defined, and the features are preserved as they cross the blade boundaries. Scheme E, which includes a second adaptation cycle on a different feature metric, further illustrates the ability of the scheme to capture and preserve complex features.

Finally, the influence of the grid adaptation on the flow field character is illustrated in Fig. 11, where Q-criterion iso-surfaces, colored by vorticity magnitude are presented. Not only are the vortex magnitudes preserved and tracks more crisply defined with the grid adaptations, but a number of distinct flow field patterns, absent with the baseline grid (11 a) can be observed. The blade vortex interaction is captured and propagates over several revolutions, while the spiral wake shed from the fuselage is also now present.

For comparison, a higher advance ratio of $\mu = 0.20$ (Table 1) was also examined. Similar results were observed for the adaptation process, as illustrated for the single vorticity magnitude grid adaptation (Scheme B) and double vorticity magnitude-pressure gradient adaptation (Scheme C). Figure 12 illustrates the mean pressures, which shows little improvement with grid adaptation compared with experiment, especially at the $x/R = 1$ location. However, as noted by Brand (Ref. 34) and confirmed computationally by O'Brien (Ref. 3), this deficiency in the pressure correlation is due to the intricacies of the hub pin rotation, which is not modeled in this effort. A better evaluation of the ability of the adaptation at this advance ratio is the examination of the unsteady peak maximum and minimums, shown in Figs. 13 and 14, respectively. The grid adaptation clearly improves the prediction of the maximum pressure peaks near the fuselage nose (Fig. 13), but little change is observed elsewhere along the fuselage centerline. The unsteady peak minimums (Fig. 14) indicate that the double adaptation of vorticity magnitude and pressure gradient improve significantly the area of interaction of the prior tip vortex and fuselage, as similarly noted for the lower advance ratio case.

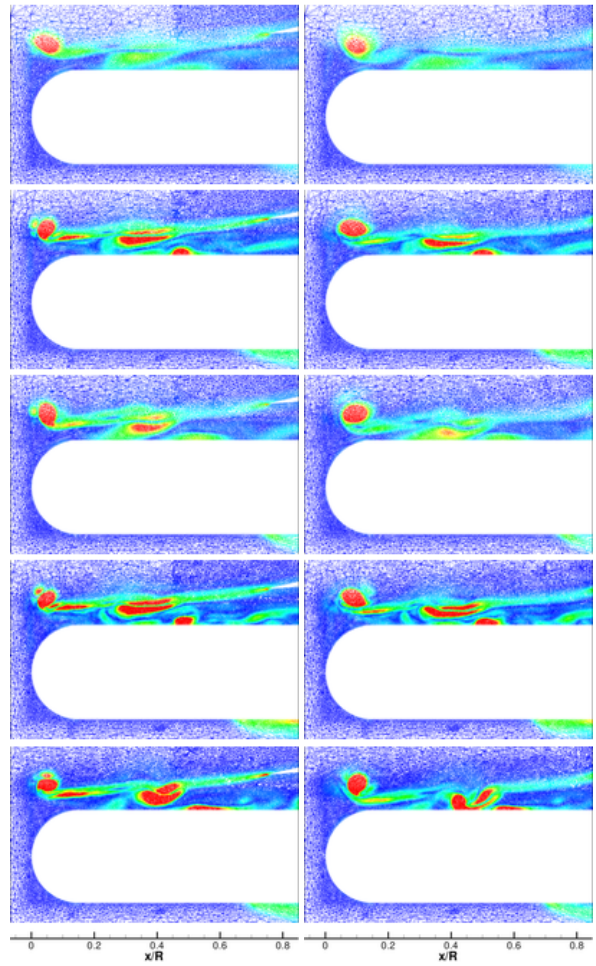

(a) $\psi = 30°$ (b) $\psi = 60°$

Fig. 7. Vortex behavior for the various adaptation schemes along the GIT fuselage symmetry plane at $\mu = 0.1$. (From top to bottom: Schemes A-E)

The interaction of the strut and hub model on the fuselage interference effects becomes more important at this advance ratio, as indicated by the correlations here.

The efficacy of the overset, time-accurate grid adaptation capability has been demonstrated, but the solution dependency on the selection of the grid feature adaptation metric is clear. In addition, the uncertainty in number of adaptation cycles suggests that a method to define convergence (rather than additional adaptation cycles) needs to be

Table 3. Summary of the different adaptation schemes utilized for $\mu = 0.2$

Scheme	Description	Grid Size
A	Initial Grid	2.03M nodes
B	Adapted to $\|\omega\|$ (1 cyc.)	6.99M nodes
C	Adapted to $\|\omega\|$ (1 cyc.) & ∇p (1 cyc.)	12.7M nodes

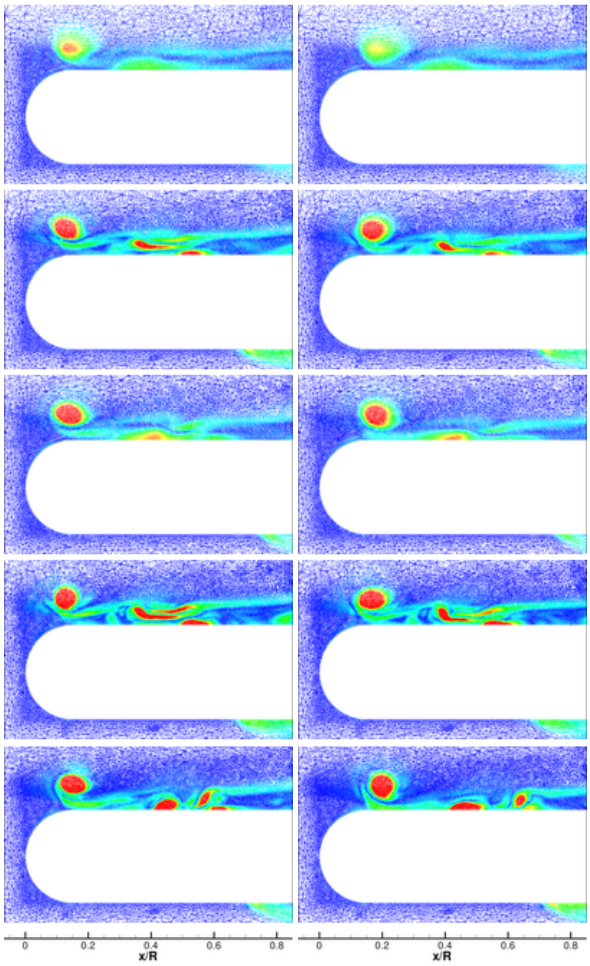

(a) $\psi = 90°$ (b) $\psi = 120°$

Fig. 8. Vortex behavior for the various adaptation schemes along the GIT fuselage symmetry plane at $\mu = 0.1$. (From top to bottom: Schemes A-E)

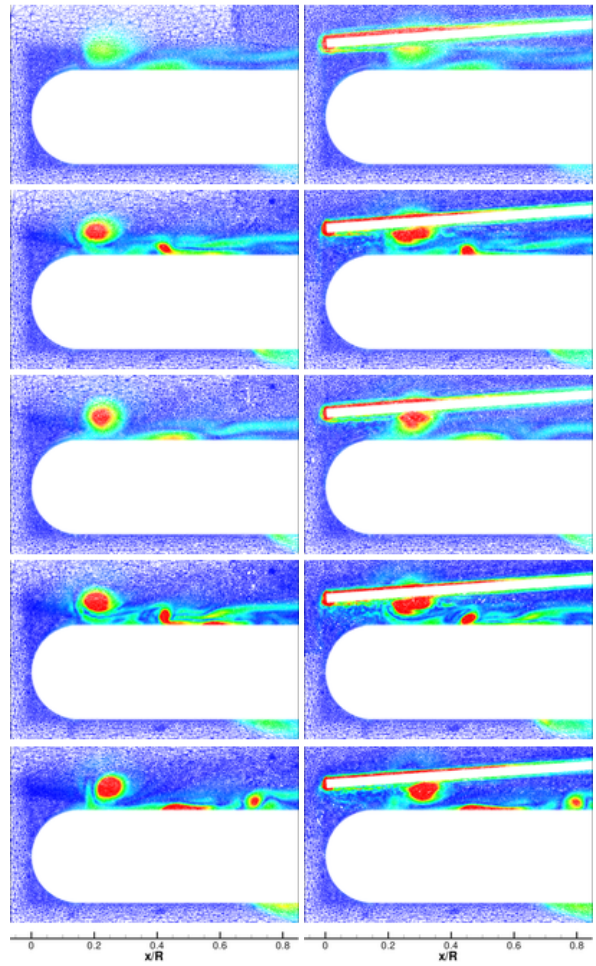

(a) $\psi = 120°$ (b) $\psi = 180°$

Fig. 9. Vortex behavior for the various adaptation schemes along the GIT fuselage symmetry plane at $\mu = 0.1$. (From top to bottom: Schemes A-E)

determined. The application of adaptation using adjoint methods may be a solution. Adjoint adaptation has been demonstrated for steady, single grids by Park and associated authors (Refs. 18, 33, 38). Extension of adjoint adaptation to include overset, time-accurate simulation capability may be warranted.

ROBIN Wake Visualization Demonstration Case

The second demonstration case is based on the ROtor Body INteraction (ROBIN) configuration, developed by NASA, which has been extensively used in various experiments and computational studies on rotor-fuselage interactions and wake trajectories (Refs. 5, 39–42). This streamlined slender ROBIN fuselage model, described by a set algebraic equations at various fuselage locations, yields a simple analytical definition for a fuselage geometry. An engine mount or "doghouse" is a characteristic feature included in the configuration. An internally mounted rotor system is utilized consisting of four blades that are fully-articulated with a NACA-0012 airfoil section. The current effort focuses on the set of experiments conducted by Ghee and Elliott (Ref. 40) in the 14-by-22-Foot Subsonic Tunnel at NASA Langley Research Center using the 2-m rotor test system (2MRTS). One of the experimental wake visualization cases (Table 4) was employed here to evaluate the influence of the adaptation process. Once again, the length data have been nondimensionalized by the rotor radius (R) to facilitate ease in interpreting the simulations.

The compressible viscous option within FUN3D was applied to the ROBIN demonstration. Similar to the GIT computations, the time step equivalency of 1° was chosen with 25 sub-iterations. Ten turbulence sub-iterations were also applied to converge the loosely-coupled Menter's kω-SST turbulence model. Here the time window for the time-dependent metric corresponded to 90° blade sweep or 90 steps. Trim angles that were previously obtained on the same grid in Smith et al. (Ref. 5) were used to estimate the required trim. The thrust values obtained were ascertained

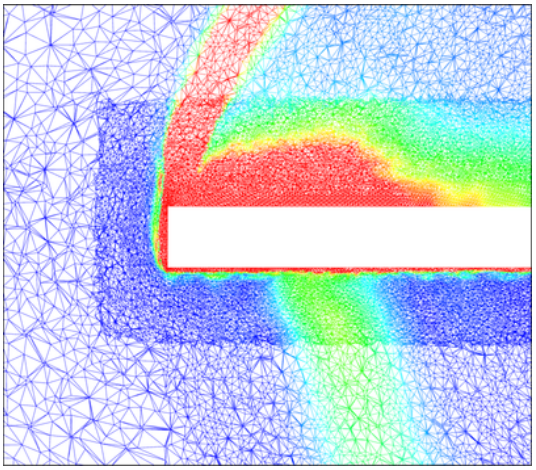

(a) Scheme A

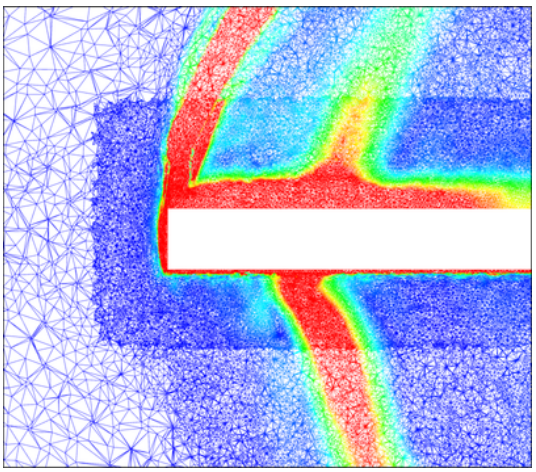

(b) Scheme B

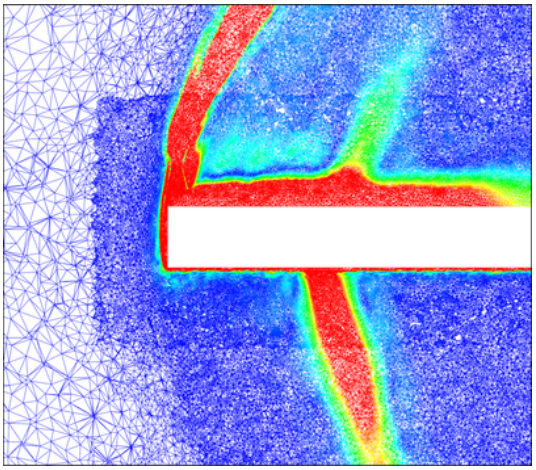

(c) Scheme E

Fig. 10. Mesh colored by vorticity contours demonstrating BVI-effect for the GIT configuration at $\mu = 0.1$.

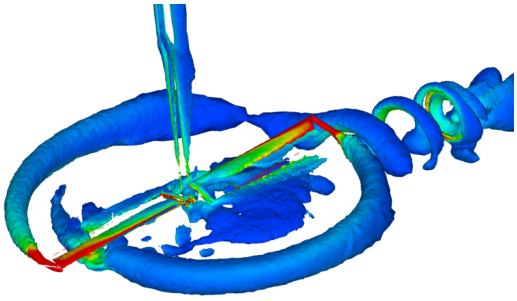

(a) Scheme A

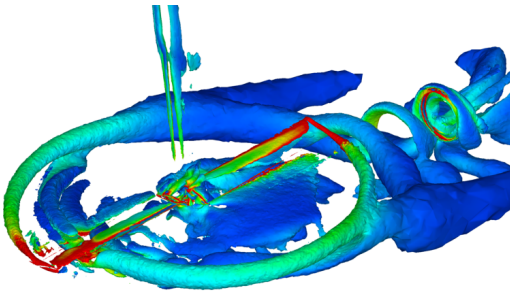

(b) Scheme B

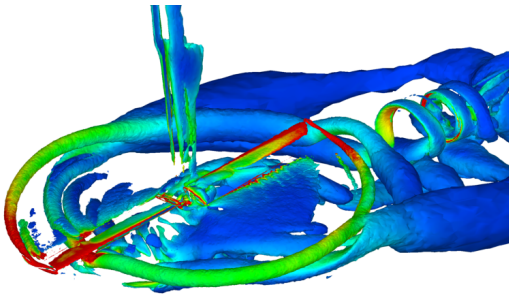

(c) Scheme E

Fig. 11. Q-criterion iso-surfaces colored by vorticity magnitude for the GIT RFI configuration at $\mu = 0.1$.

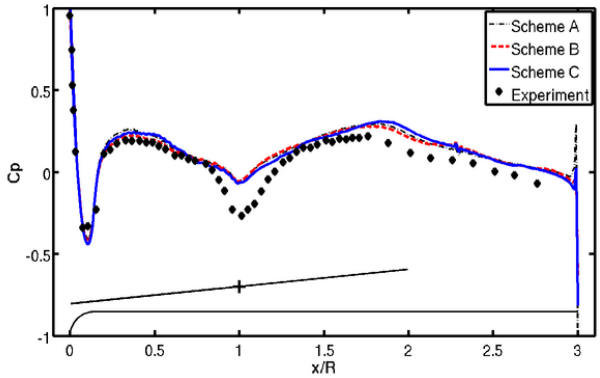

Fig. 12. Comparison of the time-averaged pressure distributions on the top centerline of the GIT airframe at $\mu = 0.2$.

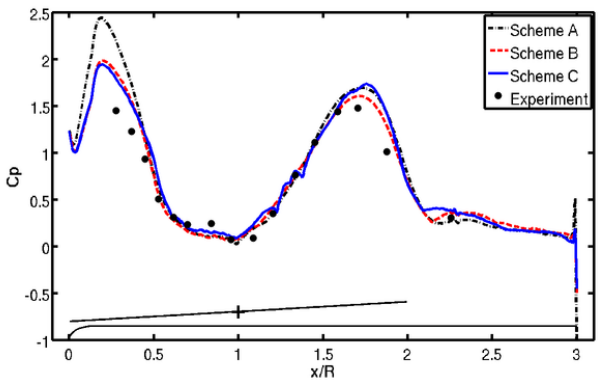

Fig. 13. Comparison of the unsteady positive peak pressures on the top centerline of the GIT airframe at $\mu = 0.2$.

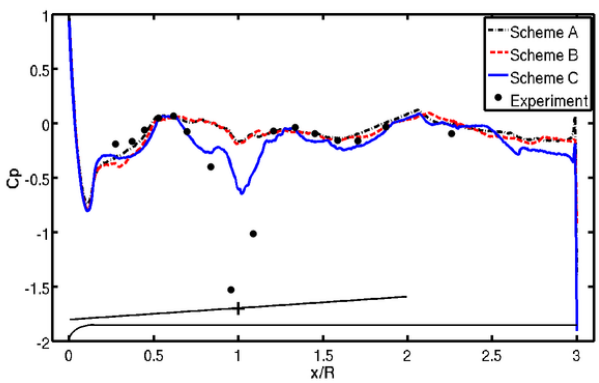

Fig. 14. Comparison of the unsteady negative peak pressures on the top centerline of the GIT airframe at $\mu = 0.2$.

to be within 2% of the experimental values listed in Table 4, which validate the correlations with experiment without further trimming the rotor.

The purpose of this demonstration case was to examine the influence of grid adaptation on the prediction of the wake vortex trajectories. To examine this, a baseline grid wake trajectory was compared to a single adaptation based on vorticity magnitude. The application of only a single adaptation with the selection of the vorticity magnitude as the adaptation metric was based on the prior GIT RFI simulations for the range of experimental data available for correlation. The initial grid had 14.4 M nodes and the vorticity based adaptation increased the size to 17.6 M nodes.

Table 4. Relevant parameters for the ROBIN wake visualization test case. (Note: All angles are reported in degrees.)

μ	C_T	α_s	β_0	θ_0	θ_{1s}	θ_{1c}
0.23	0.0064	-3.0	1.5	6.5	-3.2	-1.1

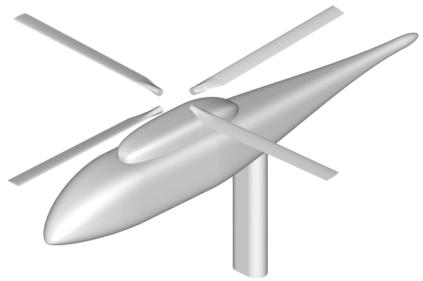

Fig. 15. Computational model of the ROBIN 2MRTS configuration.

Vorticity tracks were extracted at different longitudinal slices spanning the rotor disk. Vortex cores are determined by mapping local maxima of the normal vorticity component on each of these planes. There was no attempt made to differentiate individual vortex structures like tip vortices from these contour maps. The wake trajectories for the advance ratio of 0.23 (Fig. 16) are observed to be very similar to the experiment and the baseline grid trajectories. The major influence of the grid adaptation was not readily transparent, as it was apparent primarily in the process through which the wake trajectories were numerically determined. As discussed with the GIT demonstration case, and illustrated here via Q-criterion plots (Fig. 17), the effect of the grid adaptation was to further refine the vorticity throughout the flow field. Thus, the refined strength and minimized extent of the vortex path rendered the wake tracking much simpler and with fewer approximations.

Conclusions

A new grid adaptation strategy has been developed and demonstrated to permit time-dependent adaptation across overset, unstructured meshes. The strategy has been successfully demonstrated on two rotor-fuselage interaction configurations of interest to the rotorcraft community. In particular, the following observations can be made:

1. Overset grid adaptation to include any grid has been demonstrated using a strategy to identify and track the grid that each node is located within, along with an adaptation strategy that has been successful for single grids.

2. Demonstration on two rotor-fuselage interaction cases illustrate the solution dependency on the selection of the adaptation metric and the number of grid adaptations.

3. Flow field features and fuselage pressures require a minimum of two grid adaptation cycles. The most ac-

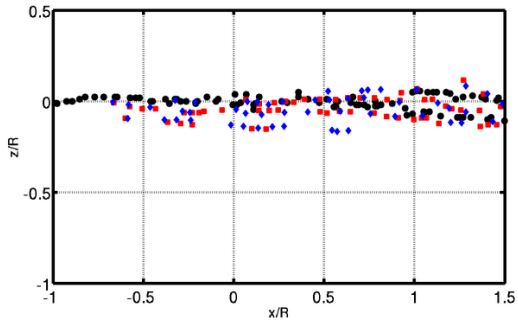

(a) $y/R = -0.3$

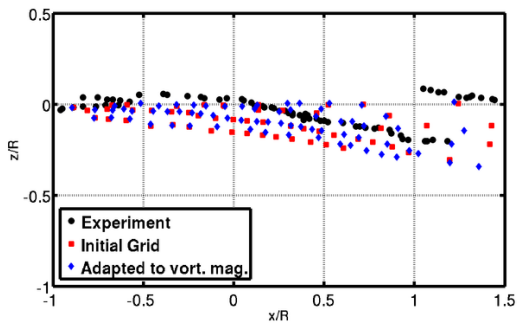

(b) $y/R = 0.3$

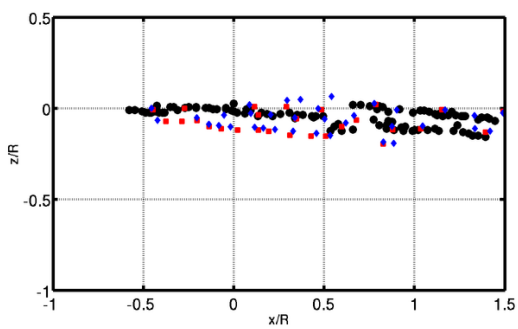

(c) $y/R = -0.8$

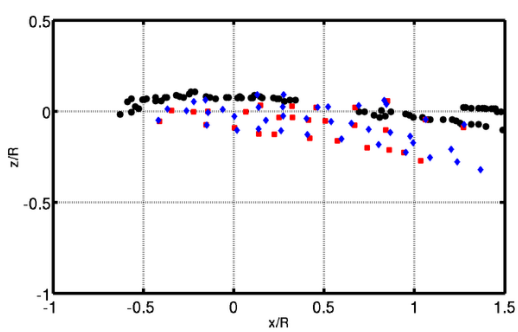

(d) $y/R = 0.8$

Fig. 16. ROBIN sideline vortex trajectories at $\mu = 0.23$.

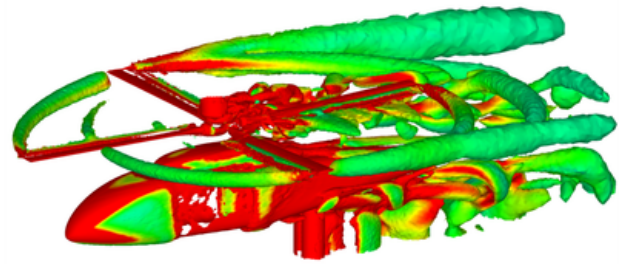

(a) Initial Grid

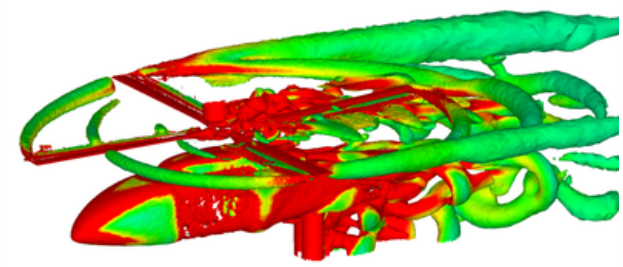

(b) Adapted Grid

Fig. 17. Q-criterion iso-surfaces colored by vorticity magnitude for the ROBIN configuration at $\mu = 0.23$.

curate adaptation metrics are vorticity magnitude followed by pressure gradient.

4. Given a sufficient baseline grid, wake trajectories of the tip vortex can be readily obtained with one adaptation cycle using vorticity magnitude as the metric.

5. The uncertainty associated with the selection of the adaptation metric and the number of adaptation cycles imply that a more rigorous adaptation process, such as adjoint adaptation, may be more appropriate than feature-based adaptation. Future efforts will focus on the development of an adaptation process that will circumvent the issues identified with feature-based adaptation, as well as extension of the method to other rotorcraft-related applications.

Acknowledgments

A portion of this research has been supported by the Department of the Navy, Office of Naval Research under grant N00014-09-1-1019, titled ”Deconstructing Hub Drag”. Dr. Judah Milgram is the technical monitor. Computational support was provided through the DoD High Performance Computing Centers at ERDC through an HPC grant from the US Navy. Any opinions, findings, and conclusions or recommendations expressed in this material are those of the author(s) and do not necessarily reflect the views of the Department of the Navy or the Office of Naval Research.

The authors would like to especially acknowledge and thank the NASA FUN3D development team, in particular Dr. Michael Park and Dr. Eric Nielsen, who pioneered the

grid adaptation efforts within FUN3D. Without their discussions, ideas, and suggestions, this effort would not have been possible.

References

[1]Ruffin, S., O'Brien, D., Smith, M., Hariharan, N., Lee, J., and Sankar, L., "Comparison of Rotor-Airframe Interaction Utilizing Overset Unstructured Grid Techniques," Proceedings of the 42nd AIAA Aerospace Sciences Meeting and Exhibit, Jan 2004.

[2]O'Brien, D., and Smith, M., "Understanding the Physical Implications of Approximate Rotor Methods Using an Unstructured CFD Method," Proceedings of the 31st Annual European Rotorcraft Forum, Sep 2005.

[3]O'Brien, D. M., *Analysis of Computational Modeling Techniques for Complete Rotorcraft Configurations*, Ph.D. thesis, Georgia Institute of Technology, 2006.

[4]Potsdam, M., Smith, M., and Renaud, T., "Unsteady Computations of Rotor-Fuselage Interactions," Proceedings of the 35th Annual European Rotorcraft Forum, Sep 2009.

[5]Smith, M.J., Shenoy, R., Kenyon, A.R., and Brown, R.E., "Vorticity Transport and Unstructured RANS Investigation of Rotor-Fuselage Interactions," Proceedings of the 35th Annual European Rotorcraft Forum, Sep 2009.

[6]Komerath, N., Smith, M. J., Tung, C., "A Review of Rotor Wake Physics and Modeling," *Journal of the American Helicopter Society*, Vol. to appear, 2011.

[7]Kang, H.J. and Kwon, O.J., "Effect of Wake Adaptation on Rotor Hover Simulations Using Unstructured Meshes," *Journal of Aircraft*, Vol. 38, (5), 2001.

[8]Kang, H.J. and Kwon, O.J., "Unstructured Mesh Navier-Stokes Calculations of the Flow Field of a Helicopter Rotor in Hover," *Journal of the American Helicopter Society*, Vol. 47, (2), 2002.

[9]Dindar, M., Shepherd, M., Flaherty, J., and Jansen, K., "Adaptive CFD analysis for rotorcraft aerodynamics," *Computer Methods in Applied Mechanics and Engineering*, Vol. 189, (4), 2000.

[10]Potsdam, M. and Mavriplis, D., "Unstructured Mesh CFD Aerodynamic Analysis of the NREL Phase VI Rotor," 47th AIAA Aerospace Sciences Meeting, Jan 2009.

[11]Park, Y.M. and Kwon, O.J., "Simulation of Unsteady Rotor-Fuselage Interactions Using Unstructured Adaptive Sliding Meshes," *Journal of the American Helicopter Society*, Vol. 49, (4), 2006.

[12]Cavallo, P.A., Sinha, N., and Feldman, G.M., "Parallel Unstructured Mesh Adaptation Method for Moving Body Applications," *AIAA Journal*, Vol. 43, (9), 2005.

[13]Meakin, R.L., "On adaptive refinement and overset structured grids," Proceedings of the 13rd AIAA Computational Fluid Dynamics Conference, June 1997.

[14]Henshaw, W.D., and Schwendeman, D.W., "Parallel Computation of Three-dimensional Flows Using Overlapping Grids with Adaptive Mesh Refinement," *Journal of Computational Physics*, Vol. 227, (16), 2008.

[15]Kannan, R., and Wang, Z.J., "Overset Adaptive Cartesian/Prism Grid Method for Stationary and Moving-Boundary Flow Problems," *AIAA Journal*, Vol. 45, (7), 2007.

[16]Canonne, E., Benoit, C., and Jeanfaivre, G., "Cylindrical mesh adaptation for isolated rotors in hover," *Aerospace Science and Technology*, Vol. 8, (1), 2004.

[17]Duque, E.P.N., Biswas, R. and Strawn, R.C., "A Solution Adaptive Structured/Unstructured Overset Grid Flow Solver with Applications to Helicopter Rotor Flows," Proceedings of the 13rd AIAA Applied Aerodynamics Conference, June 1995.

[18]Park, M.A. and Darmofal, D.L., "Parallel Anisotropic Tetrahedral Adaptation," Proceedings of the 46th AIAA Aerospace Sciences Meeting and Exhibit, Jan 2008.

[19]Lee-Rausch, E.M., Park, M.A., Jones, W.T., Hammond, D.P, and Nielsen, E.J., "Application of Parallel Adjoint-Based Error Estimation and Anisotropic Grid Adaptation for Three-Dimensional Aerospace Configurations," Proceedings of the 23rd AIAA Applied Aerodynamics Conference, June 2005.

[20]Jones, W.T., Nielsen, E.J. and Park, M.A., "Validation of 3D Adjoint Based Error Estimation and Mesh Adaptation for Sonic Boom Prediction," Proceedings of the 44th AIAA Aerospace Sciences Meeting and Exhibit, Jan 2006.

[21]Bibb, K.L., Gnoffo, P.A., Park, M.A. and Jones, W.T. , "Parallel, Gradient-Based Anisotropic Mesh Adaptation for Re-entry Vehicle Configurations," Proceedings of the 9th AIAA/ASME Joint Therophysics and Heat Transfer Conference, Jun 2006.

[22]Sankaran, V., Sitaraman, J., Wissink, A., Datta, A., Jayaraman, B., Potsdam, M., Mavriplis, D., Yang, Z., O'Brien, D., Saberi, H., Cheng, R., Hariharan, N., and Strawn, R., "Application of the Helios Computational Platform to Rotorcraft Flowfields," Proceedings of the 48th AIAA Aerospace Sciences Meeting and Exhibit, Jan 2010.

[23]Wissink, A.M., Kamkar, S., Pulliam, T.H., Sitaraman, J., and Sankaran, V., "Cartesian Adaptive Mesh Refinement for Rotorcraft Wake Resolution," Proceedings of the 28th AIAA Applied Aerodynamics Conference, June 2010.

[24]Wissink, A., Potsdam, M., Sankaran, V., Sitaraman, J., Yang, Z., and Mavriplis, D. J., "A Coupled Unstructured-Adaptive Cartesian CFD Approach for Hover Prediction," Proceedings of the 66th Annual Forum of the American Helicopter Society, May 2010.

[25]Sterenborg, v. Z. A., J.J.H.M. and Bijl, H., "Solution Based Mesh Adaptation Applied to Fluid Structure Interaction Computations," 47th AIAA Aerospace Sciences Meeting, Jan 2009.

[26]Alauzet, F. and Olivier, G., "Extension of Metric-Based Anisotropic Mesh Adaptation to Time-Dependent Problems Involving Moving Geometries," Proceedings of the 49th AIAA Aerospace Sciences Meeting and Exhibit, Jan 2011.

[27]Anderson, W., Rausch, R., and Bonhaus, D., "Implicit/Multigrid Algorithms for Incompressible Turbulent Flows on Unstructured Grids," *Journal of Computational Physics*, Vol. 128, (2), 1996.

[28]Chorin, A., "A Numerical Method for Solving Incompressible Viscous Flow Problems," *Journal of Computational Physics*, Vol. 135, (2), 1997.

[29]Roe, P., "Approximate Riemann Solvers, Parameter Vectors, and Difference Schemes," *Journal of Computational Physics*, Vol. 43, (2), 1981.

[30]Menter, F., "Two-Equation Eddy-Viscosity Turbulence Models for Engineering Applications," *AIAA Journal*, Vol. 32, (8), 1994.

[31]Noack, R., Boger, D., Kunz, R., and Carrica, P., "SUGGAR++: An Improved General Overset Grid Assembly Capability," Proceedings of the 19th AIAA Computational Fluid Dynamics Conference, June 2009.

[32]Noack, R., "DiRTlib: A Library to Add an Overset Capability to Your Flow Solver," Proceedings of the 17th AIAA Computational Fluid Dynamics Conference, June 2005.

[33]Park, M. A., *Anisotropic Output-Based Adaptation with Tetrahedral Cut Cells for Compressible Flows*, Ph.D. thesis, Massachusetts Institute of Technology, 2008.

[34]Brand, A. G., *An Experimental Investigation of the Interaction Between a Model Rotor and Airframe in Forward Flight*, Ph.D. thesis, Georgia Institute of Technology, 1989.

[35]Mavris, D. N., *An Analytical Method for the Prediction of Unsteady Rotor/Airframe Interactions in Forward Flight*, Ph.D. thesis, Georgia Institute of Technology, 1988, revised 1991.

[36]O'Brien, D., and Smith, M., "Analysis of Rotor-Fuselage Interactions Using Various Rotor Models," Proceedings of the 43rd AIAA Aerospace Sciences Meeting and Exhibit, Jan 2005.

[37]Lee, J. and Kwon, O.J., "Predicting Aerodynamic Fuselage Interactions by Using Unstructured Meshes," *Transactions of the Japanese Society for Aeronautical and Space Sciences*, Vol. 44, (146), 2002.

[38]Park, M.A. and Carlson, J.R., "Turbulent Output-Based Anisotropic Adaptation," Proceedings of the 48th AIAA Aerospace Sciences Meeting and Exhibit, Jan 2010.

[39]Mineck, R. and Althoff Gorton, S., "Steady and Periodic Pressure Measurements on a Generic Helicopter Fuselage Model in the Presence of a Rotor," Technical Report NASA/TM-2000-210286, June 2000.

[40]Ghee, T.A. and Elliott, J.W., "The Wake of a Small-Scale Rotor in Forward Flight Using Flow Visualization," *Journal of the American Helicopter Society*, Vol. 40, (3), 1995.

[41]Park, Y.M., Nam, H.J, and Kwon, O.J., "Simulation of Unsteady Rotor-Fuselage Interactions Using Unstructured Adaptive Meshes," *Journal of the American Helicopter Society*, Vol. 51, (2), 2006.

[42]Kenyon, A.R. and Brown, R.E., "Wake Dynamics and Rotor-Fuselage Aerodynamic Interactions," *Journal of the American Helicopter Society*, Vol. 54, (1), 2009.